COMPARISON OF ROTOR STRUCTURAL AND AERODYNAMIC LOADS USING THE HART II TEST DATA

Sung Nam Jung, Jae-Sang Park, Young-Hyun You, Yung Hoon Yu, Jee-Woong Kim
Soo-Hyung Park
Department of Aerospace Information Engineering, Konkuk University
Hwayang-dong, Gwangjin-gu, Seoul 143-701, KOREA

Do-Hyung Kim
Rotor Department, Korea Aerospace Research Institute
45 Eoeun-dong, Yuseong-gu, Daejeon 305-333, KOREA

Abstract

In the present work, the comprehensive structural dynamics (CSD) analysis codes including DYMORE and CAMRAD II are used to evaluate the accuracy of the aeroelastic analysis solution as well as to validate the higher harmonic control aeroacoustic rotor test (HART) II data obtained for the aerodynamic and structural loads of the model-scale BO-105 helicopter in descending flight condition. A total of 16 finite elements along with 17 aerodynamic panels are used for the CAMRAD II analysis, whereas in the DYMORE analysis, 10 finite elements with 31 equally-spaced aerodynamic panels are utilized. To improve the prediction capability of DYMORE analysis, the finite state dynamic inflow model is upgraded with a free vortex wake model comprised of near shed wake and trailed tip vortices. The predicted results on structural dynamics analysis, aerodynamic loads, blade motions, and structural loads are correlated with the HART II measurement data for the baseline (BL), minimum noise (MN), and minimum vibration (MV) cases. It is found that an improvement of solution, especially for BVI (Blade Vortex Interaction) airloads, is achieved with the free wake method employed in the DYMORE analysis. Overall, fair to good correlation is achieved for the test cases considered in this study.

1. INTRODUCDTION

The blade vortex interaction (BVI) is caused by interaction between the rotor blades and their trailed wakes and this occurs mainly in low speed transition flight and causes significant noise and vibration problem. In order to improve basic understanding for the formation of vortex wakes and their interaction leading to noise and vibration, an international cooperative program HART II was conducted in 2001 [1], following the previous HART I [2]. Particularly, the goals were to measure the noise level, airloads, vortex wakes, and blade motions with and without higher harmonic pitch control (HHC) inputs.

After the test, a significant volume of research has been conducted for prediction of BVI airloads and structural loads in reference to the measurement data constructed by HART II program. The analyses range from low-order CSD (Comprehensive Structural Dynamics) methods [3-6], hybrid methods [7], and more sophisticated loose/tight CSD/CFD coupled approaches [8-10]. It is recognized that a CSD/CFD coupled analysis is desirable to capture well the BVI phenomena and to obtain accurate aeroelastic solutions. However, this requires heavy computing resources even with the state-of-the-art solution technologies. Computationally more efficient methodologies yielding reasonable accuracy solution are always needed for a practical usage, especially at preliminary design stage. In this regard, a lifting-line based CSD approach equipped with free vortex wake model still deserves to be taken into consideration. The computed results from CSD analysis can be used as a datum at the stage of comparing and assessing the prediction capability of state-of-the-art analysis methods.

Recently, flexible multibody dynamics modeling techniques attract growing attention for use in rotorcraft applications. One of them is DYMORE that has been developed by Bauchau [11]. DYMORE uses geometrically exact beam theory [12] for nonlinear elastic beam model and the finite-state dynamic inflow model [13] for the aerodynamic model. The inflow model is relatively simple to estimate the complex rotorcraft flow field and more refined representation of aerodynamics is required for more enhanced prediction [7,14].

In order to improve the rotor wake modeling capability, Roget [15] incorporated a time marching free vortex wake method developed by B-L (Bhagwat and Leishman) [16] into DYMORE. This model has

been applied to investigate the control authority of the active twist rotor and the active trailing-edge flap mechanism for a scaled rotor model.

In the present work, the prediction capability of DYMORE with the B-L free vortex wake model is assessed for the evaluation of BVI airloads, blade motions, and structural loads of HART II rotor with and without harmonic control inputs. The comprehensive aeroelastic analysis code CAMRAD II [17] is also employed to cross-check the validity of blade modeling and to gain confidence about DYMORE predictions. Both the CSD predictions on airloads and structural responses of the rotor are correlated with the test data for the baseline (BL), minimum noise (MN), and minimum vibration (MV) cases.

Numerous collection of conference proceeding papers and journal articles are listed in the official HART II web site [18]. Since most of the research is focused on the aerodynamic and the aeroacoustic aspects of the rotor, there is clearly a lack of published efforts on the structural dynamics aspects of the rotor. A few exceptions are Lim et al. [3], Lim [10], and Ganguli et al. [19]. These mainly rely on a single CSD code to validate their analysis results with measured data. The present approach uses two separate CSD codes to systematically validate the CSD predictions with the HART II test results and it is believed to bridge a gap in the literature toward more advanced CFD/CSD coupled aeroelastic analysis.

2. HART II TEST

The HART II test were conducted in the open-jet anechoic test chamber having a 8m x 6m cross-section in the German-Dutch wind tunnel (DNW). The rotor was in descent flight conditions with an advance ratio $\mu = 0.15$, a shaft tilt angle $\alpha_s = 5.3\,\mathrm{deg}$. (4.5 deg. after wall correction of the wind tunnel), a hover tip Mach number $M = 0.6387$ and a thrust level $C_T = 0.0044$.

For the HART II rotor, 40% Mach-scaled models of the production BO-105 hingeless rotors were fabricated. The blade was dynamically scaled to match the natural frequencies of the first three flapping modes, the first two lag modes, and the first torsion mode of full-scale versions. The chord length was increased by 10% to compensate for the Reynolds number error. The blades had rectangular planform shape with -8 deg. linear pretwist and 2.5 deg. precone. The blades had a NACA23012 airfoil with a 5.4% trailing-edge tab. The general properties of HART II blades are given in Table 1. Table 2 presents the forces and moments measured in the hub-fixed frame as well as the higher harmonic pitch inputs for the three test cases. It is noted that the roll and pitch moments are defined as positive when the advancing side goes down and when the nose-up motion is accompanied, respectively.

The cross-section of blades was composed of C-type spar, skin, and foam core. Both the skin and spar are made of glass fiber. The number 1 blade was designated as the reference blade and defined the rotor azimuth. Each blade was instrumented with six strain gauges: three for flap, two for lead-lag, and one for torsion, while the reference and opposite blades (numbered one and three) were equipped with a root pitch sensor. The pitch link loads were also measured with a strain gauge attached to the pitch links.

The deflections of HART II blades were measured optically by using the SPR (Stereo Pattern Recognition) technique. To this purpose, 18 markers were distributed along the blade span and attached at both leading and trailing edges with an equal spacing starting from 22.8% radial location. The elastic blade motion was defined with respect to the rotor hub coordinate system. Both the flap and lead-lag motions were computed at the quarter chord line. The pitch angle θ_{SPR} is obtained using the vertical distance between the two markers (Δz) and their relative length along with a correction angle as:

$$\theta_{SPR} = \arctan\frac{\Delta z}{89\mathrm{mm}} + 1.65^{\circ} \tag{1}$$

The elastic torsion ϕ is expressed in the following form by considering the pretwist angle θ_{tw} , the basic control, $\theta_0, \theta_{1c}, \theta_{1s}$, and the 3/rev harmonic pitch inputs, θ_{3c}, θ_{3s} :

$$\begin{aligned}\phi = {} & \theta_{SPR} - \theta_0 - \theta_{tw}(r - .75) - \theta_{1S}\sin\psi \\ & - \theta_{1C}\cos\psi - \theta_{3S}\sin 3\psi - \theta_{3C}\cos 3\psi\end{aligned} \tag{2}$$

where *r* is the radial distance non-dimensioned by the length of the blade.

3. CSD ANALYSIS

The comprehensive structural dynamics model used for the HART II validation is described in this section. A nonlinear flexible multi-body dynamics code DYMORE [11] as well as a comprehensive aeroelastic analysis code CAMRAD II [17] are employed to obtain the aerodynamic loads acting on the blades and the corresponding structural responses of the rotor.

3.1 DYMORE with free wake model

DYMORE is a nonlinear flexible multibody dynamics analysis system that includes rigid bodies, rigid/elastic joints, and elastic bodies such as beams, plates, and shells. It uses a geometrically exact beam theory [12] for the elastic blade representation, a two-dimensional airfoil theory with an airfoil table look-up for the aerodynamic forces and moments,

and Peters and He's finite-state dynamic inflow model [13]. This inflow model is constructed by applying the acceleration potential theory to a rotor aerodynamics problem with a skewed cylindrical wake. More specifically, the induced flow at the rotor disk is expanded in terms of modal functions. As a result, a three-dimensional, unsteady induced-flow aerodynamic model with a finite number of states is derived in time domain. This model is an intermediate level of wake representation compared with the more complicated freewake methods.

The freewake analysis is based on a potential flow with the vorticity being concentrated on a finite number of vortex filaments. The motion of a point on a vortex filament is described by the motion of Lagrangian fluid markers as:

$$\frac{d\mathbf{r}(\psi,\zeta)}{dt} = \mathbf{V}\left(\mathbf{r}(\psi,\zeta)\right) \tag{3}$$

where $\mathbf{r}$ is the position vector of the point on the vortex filament and $\mathbf{V}$ is the local fluid velocity at the point $\mathbf{r}$. In addition, ψ and ζ denote the blade azimuth angle and wake age, respectively. From Eq. (3), the vorticity transport equation is written in the following partial differential form:

$$\frac{d\mathbf{r}(\psi,\zeta)}{d\psi} + \frac{d\mathbf{r}(\psi,\zeta)}{d\zeta} = \frac{\mathbf{V}\left(\mathbf{r}(\psi,\zeta)\right)}{\Omega} \tag{4}$$

where Ω is the rotational speed. Eq. (4) dictates the governing equation for the free-vortex problem applied to the rotor wake. The left-hand-side of Eq. (4) is a one-dimensional wave equation. The complexity of the problem comes from the right-hand-side term, which is highly nonlinear. In order to solve Eq. (4), the domain (ψ, ζ) is discretized into finite steps of $\Delta\psi$ and $\Delta\zeta$. In addition, the derivatives of the left-hand-side in Eq. (4) are approximated by the finite difference scheme. The discretized equation is integrated by applying the time marching algorithm using predictor-corrector with the 2nd-order backward difference, as proposed by Bhagwat and Leishman [16] and later modified by Roget [15].

The trailed near wake is also taken into account to improve the accuracy of the solution. The near wake consists of a series of vortex filaments trailed behind the blades for a given angular distance. The trailed vortices comprise the near wakes, which are assumed to be planar with a fixed angular distance. The tip vortex that constitutes the freewake extends beyond the near wake with the strength equal to the maximum bound circulation along the blade. The strength of the blade bound vorticity is determined from the induced velocity at the control points.

The overall procedures to obtain the aerodynamic forces along the blades are described as follows: First, the aerodynamic lift is estimated by the two-dimensional strip theory using the inflow distribution obtained from the freewake model. Second, using the estimated lift, the angle of attack for the equivalent flat plate is determined. Third, the surface normal vector at the control point is adjusted to make it consistent with the equivalent flat plate angle of attack. Fourth, the blade bound circulations and the equivalent lifts are calculated. Finally, the effective angle of attack at each air station point is determined from a reverse table look-up procedure. This solution procedure allows for the circulation distribution on the blade to be consistent with the circulation released into the freewake.

3.2 CAMRAD II

CAMRAD II is a comprehensive aeromechanical analysis code that is characterized by multibody dynamics, nonlinear finite elements, and various level of rotorcraft aerodynamics [17]. For the structural analysis, the blade motion consists of the sum of the rigid body motion and the elastic deformation. The rigid body motion describes the motion of one end of a beam element, and the elastic motion is measured relative to the rigid motion. Either Euler-Bernoulli or Timoshenko level of approximations toward the beam representation is possible from the structural model depending upon the materials chosen for the blades. A quasi-static reduction of transverse shear variables is enforced to keep the number of degrees of freedom identical in both the beam approximations.

The aerodynamic model used in CAMRAD II is based on a lifting-line theory using steady two-dimensional airfoil characteristics and the vortex wake. Several different attached-flow unsteady aerodynamics along with various dynamic stall models are implemented in CAMRAD II. For the vortex wake model, the free wake geometry is used to compute the non-uniform induced inflow distribution around the rotor disk. The tip vortex formation is modeled using a rolled-up wake model that is constructed from the magnitude and position of peak bound circulation [4].

4. RESULTS AND DISCUSSION

Both the DYMORE and CAMRAD II predictions of the HART II rotor are correlated with the wind tunnel measurement data. The test conditions considered for the HART II validation include the baseline (BL), minimum noise (MN), and minimum vibration (MV) cases. For both the MN and MV cases, 3/rev HHC inputs with different phase shift angles are added to the pitch controls (see Table 2).

4.1 Structural dynamics modeling and analysis

For the CSD predictions, the blades are divided into a series of smaller beam segments. Fig. 1 shows the finite element models used in the CAMRAD II and

the DYMORE analysis for the HART II blades. For the CAMRAD II analysis, a total of 16 beam elements comprised of 12 elements in the inboard region and the other 4 in the main blade are used to model the blade. Whereas in the DYMORE analysis, 10 equally-spaced beam finite elements except the inner-most element before the feathering hinge location are utilized. The reason of distributing finer elements in the inboard region is to address the non-uniform distribution of blade spanwise properties of HART II blades and to obtain more accurate structural responses in that region.

Figure 2 shows the four-bladed structural model used for the DYMORE analysis. Due to insufficient information about the control system components of HART II rotor, only the blades and rotor hub are modeled in the CSD analysis. Instead, to simulate the HART II rotor configuration realistically, a feathering hinge is incorporated and modeled with a revolute joint. An artificial torsion spring is attached to this feathering hinge joint. The torsion spring constants are varied to match the control system stiffness of HART II blades. The rotor hub is modeled as a rigid body and connected with a revolute joint, as denoted in Fig. 2.

Using the structural models described above, the free vibration analysis of rotating HART II blades in vacuum condition is conducted. Figures 3 and 4 present comparison results of fan plot obtained for the first five frequencies and their corresponding mode shapes, respectively, between the two CSD predictions and the HART II documentation data [18]. It should be mentioned that, regarding the HART II documentation data, the non-rotating frequencies are measured, while the rotating frequencies along with the mode shapes are computed using DLR's S4 code [6]. The natural frequencies and rotating speeds are non-dimensionalized by the rotor nominal speed, Ω = 109.0 rad/s, while the amplitudes of each mode shape are non-dimensionalized by its maximum values at the blade tip. Overall, the predicted free vibration results are in good agreement with the HART II documentation data. The maximum errors are within 5% compared with the documentation data. It is noted that the first torsion frequencies are adjusted to match those of the HART II documentation data. A spring constant amounting 1000 N-m/rad is used to this purpose. Both the CAMRAD II and DYMORE predictions lead to almost identical results for flap and lead-lag modes but show slight variations for the torsion mode. The two noticeable kinks found in the torsion mode correspond to the feathering hinge and blade cut-out locations, respectively.

4.2 Aerodynamic loads

The predicted airloads obtained for the three test cases in descending flight condition are compared with the wind tunnel measurement records [18]. Both the predictions by DYMORE with B-L free wake model and CAMRAD II with roll-up wake model are correlated with the measured data. Table 3 summarizes the comparison of computed pitch control inputs obtained using CAMRAD II and DYMORE for each of the three test conditions. The pitch control inputs are obtained after the trim iterations are converged. The target values for the trim are given in Table 2.

Figure 5 shows the effect of different inflow models employed in the DYMORE analysis on the section normal force, M^2C_n, and pitching moments, M^2C_m, at 87% radial station for the BL case. The measurement data are also included for comparison purpose. The measured data shows strong BVIs in the advancing and retreating sides. It is seen that the predicted DYMORE results with a finite-state dynamic inflow model do not capture the BVI event along the azimuths. This is because the inflow model is based on simple harmonic functions and cannot describe high frequency BVI oscillations. Whereas, the free wake model improves the correlation drastically, especially at or near BVI events. It is notable that both the numbers and magnitudes of BVIs are captured quite nicely, but there is an apparent phase shift over the front disk area (ψ = 180 deg.). No wake model is capable of capturing BVI oscillations in the section pitching moments since the lifting-line based model cannot describe the rapid movements of center of pressure during the BVI event.

Figure 6 shows the comparison of the section normal forces (a) and pitching moments (b) between the CAMRAD II and DYMORE predictions and measured data. The solid continuous line denotes the CAMRAD II results while the dashed line denotes the DYMORE results. A time step size of 15 deg. and 1 deg. is used for CAMRAD II and DYMORE analysis, respectively. As is seen, mean airloads are reasonably predicted for both the CSD analyses, however, most of the BVI peaks are missed in the CAMRAD II predictions due to a large time step size used in the analysis. The CAMRAD II predictions show slightly better correlation for the pitching moments as compared with the measurement data.

Figure 7 presents the comparison of normal forces, M^2C_n, and pitching moments, M^2C_m, obtained at 87% span location for the MN case. As compared with the BL case, a 3/rev variation of sectional lifts is observed with the introduction of 3/rev HHC inputs. The number of measured BVI peaks becomes reduced significantly for the MN case, as compared with the absence of HHC control inputs. In general, DYMORE results with free wake model show better correlation against the measured data than the CAMRAD II predictions, especially in advancing and retreating sides. However, a phase lead problem (about 20^o) similar to that occurred in the BL case is again observed in the DYMORE results. The peak-

to-peak values of M^2C_n are reasonably captured with the CAMRAD II predictions. It is seen that there is a constant offset between the measured data and the CSD predictions for the estimation of M^2C_m.

The section normal lifts and pitching moments at 87% radial location for the MV case are investigated next. Figure 8 shows the comparison results for the section normal forces and pitching moments. It is seen that the DYMORE analysis with free wake model shows a good correlation with measured data even though several BVI peaks in the first quadrant are missed and there remains a slight phase shift problem. The CAMRAD II predictions present better correlation in the phase angles.

The alternative way to look into BVI airloads are to find the gradient of the sectional lift with respect to the time, $d(M^2C_n)/d\psi$, because the highly impulsive and rapid fluctuating lifts during BVI events lead to sharp spikes in the gradient of sectional lifts. In other words, higher M^2C_n gradients mean stronger BVIs. Figure 9 shows a comparison of sectional lift gradients between DYMORE analysis with free wake model and the measured data obtained for the three test cases. CAMRAD II results are not included because of the impractically large time step size. The time step size used for DYMORE analysis is 1 deg, whereas the experimental data has 0.176 deg. In order to compensate for the inconsistency, DYMORE results are interpolated using the cubic spline technique leading a time step of 0.25 deg. As is denoted in Fig. 9, the correlation with experimental data is generally good to fair for most cases. The BVI peaks in the advancing side are reasonably captured with the present analysis for both the BL and MV cases, but the predicted peaks of the MN case are much less impulsive compared to the measurement data. In addition, the predictions show under-estimation of BVI peaks at around 300 deg. azimuth angles for all the cases. More refined representation of aerodynamic loads seems required to enhance the correlation.

4.3 Blade motions

Figure 10 shows the comparison of time variation of flap, lead-lag, and torsion deformation at the blade tip between the measured data and the predicted results computed by CAMRAD II and DYMORE for the BL case. The blade deflections are measured at 24 azimuth positions in increments of 15^o. In order for simplicity, only the measured deflections of the reference blade (No. 1 blade) are presented, even though the experimental data show significant blade-to-blade dissimilarities [6,10]. The sign convention for each of the blade deflections is defined as positive when the blade undergoes flap-up, lag-back, and nose-up deformation, respectively. The flap deflections are obtained by removing the precone angles from the vertical displacements, while the elastic twist deformation is obtained by subtracting the pitch control inputs and pretwist angles from the total geometric pitch angle, as given in Eq. (2).

As is seen in Fig. 10, the correlation is generally good for the flap deflections, while the correlation is fair to poor for the elastic torsion and lead-lag deflections, respectively. It is indicated that there are constant offsets amounting about 1/3 chord length between the measured and predicted lead-lag deflections. This trend has also been observed in previous investigations [3,10] and similar reults are obtained in the present predictions. The DYMORE results are in better agreement with the measured flap deflections than the CAMRAD II predictions, but the peak-to-peak magnitudes of lead-lag deflections by DYMORE are larger than those with other methods. The 2/rev characteristics of the measured elastic twist deformation are captured well with the DYMORE, however the mean values are correlated better with the CAMRD II.

Figures 11 and 12 show the comparison of tip deflections in flap, lead-lag, and elastic twist deflections for the MN and MV cases, respectively. As is expected from the rotor with 3/rev HHC inputs, a clear 3/rev response is noticed for both the flap and elastic twist deformation. The correlations between the predictions and test results are generally good for flap and torsion deflections, but the lead-lag deflections show constant offsets between predicted results and measured data. For the flap response, the CAMRAD II predictions show better correlation in the MN case, but better correlation is noticed with DYMORE in the MV case, as compared with measurement data. It is indicated that the HHC inputs do not affect much on the lead-lag response. The lead-lag deflections obtained for both the MN and MV case show only a marginal difference as compared with the BL case. Except the lead-lag deflections, the analysis results slightly under-predict the peak-to-peak response compared with measured values.

4.4 Blade structural moments

So far, the detailed information about structural moments is not available from the official HART II documentation and hence the published data [10] found in the literature are used for the present validation study. For the measurement of structural loads, a total of six strain gauges are attached to the inboard region (except torsion) for each of the blades: three for the flap mode installed at 15%, 17%, and 19% radial stations, respectively, two for the lead-lag mode at 14% and 17% radial stations, respectively, and one for the torsion mode at 33% radial stations. Noted that the mean values of the structural moments were removed from the original test data and thus only the 1/rev and higher harmonic components were compared with each other.

Figure 13 shows the comparison of flap bending, lead-lag bending, and torsion moments at specified

radial locations obtained between the two predictions and measurement data. Overall, the correlation is poor for the flap bending in both magnitudes and phases, and fair to good for the lead-lag bending and torsion moment. The peak-to-peak magnitudes of the predicted flap bending moments are underestimated significantly as compared with the measured values. The unusually large variation in the measured flap bending at the two adjacent radial locations (15% and 17%) could be associated with the drastic change of sectional properties in that part of the region of the blades. However, both the CSD predictions result in only marginal variations between the two locations. For both the lead-lag and torsion moments, the CAMRAD II results show much better correlation than those with DYMORE. The larger peak-to-peak magnitudes in the predicted lead-lag bending moments by DYMORE are mainly due to the over-estimation of lead-lad deflections.

Figures 14 and 15 illustrate the correlation for the MN and MV cases, respectively. The peak-to-peak magnitudes in the estimation of flap deflections become increased significantly so that better correlations with test data are observed especially with the CAMRAD II analysis. However, significant out-of-phase problem is again met with the CSD methods. It is indicated that excellent correlations are obtained in the prediction of torsion moments in both the MN and MV cases. As in the BL case, the CAMRAD II predictions on lead-lag moments demonstrate better correlation with the measurement data in the MN and MV cases than those estimated by DYMORE.

5. CONCLUSION

In this work, the prediction capability of CSD codes including DYMORE and CAMRAD II has been demonstrated for the HART II rotor with and without HHC control inputs. The test conditions considered include the baseline (BL), minimum noise (MN), and minimum vibration (MV) cases. A B-L (Bhagwat and Leishman) free vortex wake model comprised of near shed wake and trailed tip vortices is implemented in the DYMORE analysis. It is found that the free wake model improves significantly on the BVI airloads prediction at both advancing and retreating sides compared with the finite-state dynamic inflow model. However, either CSD codes is able to capture the BVI event for section pitching moments. The gradient of airloads demonstrates reasonable correlation, but result in less impulsive responses as compared with the measured data. With regard to the blade motions, fair to good correlation is obtained with both the CSD predictions. It is indicated in the validation of structural moments that the CAMRAD II predictions correlate reasonably well with the test data except the flap moment case. A further study is required to enhance this correlation. It is believed that the current study provides a firm database for comprehensive comparison and this investigation will become a stepping stone toward more refined aeroelastic analysis such as the CFD/CSD coupled methodology.

ACKNOWLEDGEMENT

This work was supported by National Research Foundation (NRF) through a grant provided by the Korean Ministry of Education, Science & Technology (MEST) in 2009 (No. K20601000001). The authors express sincere thanks to Dr. Bauchau and Dr. Liu at Georgia Tech, and Dr. Roget at NIA for their help and advice to this work. Special thanks is given to Dr. Berend van der Wall at DLR, Germany, and all participating members of the HART II test team for their invaluable collaborative efforts.

REFERENCES

[1] B. G. van der Wall, “2nd HHC Aeroacoustic Rotor Test (HART II) - Part I: Test Documentation - Institute Report IB 111-2003/31,” *German Aerospace Center (DLR)*, Braunschweig, Germany, Nov. 2003.

[2] Y.-H. Yu, et al., “The HART-II Test: Rotor Wakes and Aeroacoustics with Higher-Harmonic Pitch Control (HHC) Inputs - The Joint German/French/Dutch/US Project,” *58th Annual AHS Forum*, Montreal, Canada. June 11-13, 2002.

[3] J.-W. Lim, et al., “HART II: Prediction of Blade-Vortex Interaction Loading,” *29th European Rotorcraft Forum*, Friedrichshafen, Germany, Sept. 16-18, 2003.

[4] H. Yeo, and W. Johnson, “Assessment of Comprehensive Analysis Calculation of Airloads on Helicopter Rotors,” *Journal of Aircraft*, Vol. 42, No. 5, 2005, pp. 1218-1228.

[5] J.-W. Lim, and B. G. van der Wall, “Investigation of the Effect of a Multiple Trailer Wake Model for Descending Flights,” *61st Annual AHS Forum*, Grapevine, Texas, June 1-3, 2005.

[6] B. G. van der Wall, and J. Yin, “DLR’s S4 Rotor Code Validation with HART II Data: The Baseline Case,” *Int. Forum on Multidisciplinary Technology*, Seoul, Korea, Oct. 15-17, 2007.

[7] B.-Y. Min, L. N. Sankar, J. V. R. Prasad, and D. Schrage, “A Physics-based Investigation of Gurney Flaps for Rotor Vibration Reduction,” *65th Annual AHS Forum*, Grapevine, Texas, May 27-29, 2009.

[8] M. Potsdam, H. Yeo, and W. Johnson, “Rotor Airloads Prediction using Loose Aerodynamic/ Structural Coupling,” *Journal of Aircraft*, Vol. 43, No. 3, 2006, pp. 732-742.

[9] C. Yang, Y. Inada, and T. Aoyama, “BVI Noise Prediction using HART II Motion Data,” *Int. Forum on Multidisciplinary Technology*, Seoul, Korea, Oct. 15-17, 2007.

[10] J.-W. Lim, “An Assessment of Rotor Dynamics Correlation for Descending Flight using CSD/CFD Coupled Analysis,” *64th Annual AHS Forum*, Montreal, Canada, Apr. 29-May 1, 2008.

[11] O. A. Bauchau, DYMORE User’s Manual, Georgia Institute of Technology, USA, Feb. 2007.

[12] D. H. Hodges, “A Mixed Variational Formulation Based on Exact Intrinsic Equations for Ddynamics of Moving Beams,” *International Journal of Solids and*

Structures, Vol. 26, 1990, pp. 1253-1273.
[13] D. A. Peters, and C. J. He, "Finite State Induced Flow Models Part II: Three-Dimensional Rotor Disk," *Journal of Aircraft*, Vol. 32, No. 2, 1995, pp. 323-333.
[14] H. Liu, Interfacing Comprehensive Rotorcraft Analysis with Advanced Aeromechanics and Vortex Wake Models, Ph.D Thesis, Georgia Institute of Technology, USA, 2008.
[15] B. Roget, "Simulation of Active Twist and Active Flap Control on a Model-scale Helicopter Rotor," *24th Applied Aerodynamics Conference*, San Francisco, CA, June 5-8, 2006.
[16] M. J. Bhagwat, and J. G. Leishman, "Stability, Consistency and Convergence of Time-marching Free-vortex Rotor Wake Algorithms," *Journal of the American Helicopter Society*, Vol. 46, 2001, pp. 59-71.
[17] W. Johnson, "CAMRAD II, Comprehensive Analytical Model of Rotorcraft Aerodynamics and Dynamics," Johnson Aeronautics, Palo Alto, CA, 1992.
[18] B. G. van der Wall, 2nd HHC Aeroacoustic Rotor Test (HART II) - Part I: Test Documentation, Institute Report IB 111-2003/31, German Aerospace Center (DLR), Braunschweig, Germany, 2003.
[19] A. A. Kumar, S. R. Viswamurthy, and R. Ganguli, Correlation of Helicopter Rotor Aeroelastic Response with HART II Wind Tunnel Test, *35th European Rotorcraft Forum*, Liverpool, UK, 2008.

TAB 1. General properties of HART II rotor blades.

Properties	Values
Number of blades, N	4
Radius, R	2.0 m
Root cutout	0.44 m
Chord length, c	0.121 m
Solidity, σ	0.077
Blade mass	2.24 kg
Lock number	8.06
Nominal rotor speed, Ω	1041 rpm

TAB 2. Measured forces and moments, and higher harmonic control inputs for the test cases.

	BL	MN	MV
Thrust, N	3,300	3,300	3,290
Roll moment, Nm	20	30	20
Pitch moment, Nm	-20	-30	-30
θ_{3c}	0^o	0.41^o	-0.79^o
θ_{3s}	0^o	-0.70^o	0.00^o

TAB 3. Trim analyses results for baseline (BL), minimum noise (MN), and minimum vibration (MV) cases.

	BL		MN		MV	
	C-II*	Dym*	C-II*	Dym*	C-II*	Dym*
θ_0	3.68	3.69	3.81	3.71	3.62	3.71
θ_{1c}	1.16	2.06	1.33	2.05	1.16	2.10
θ_{1s}	-1.40	-1.11	-1.37	-1.20	-1.44	-1.17

* C-II and Dym are acronyms for CAMRAD II and DYMORE, respectively.

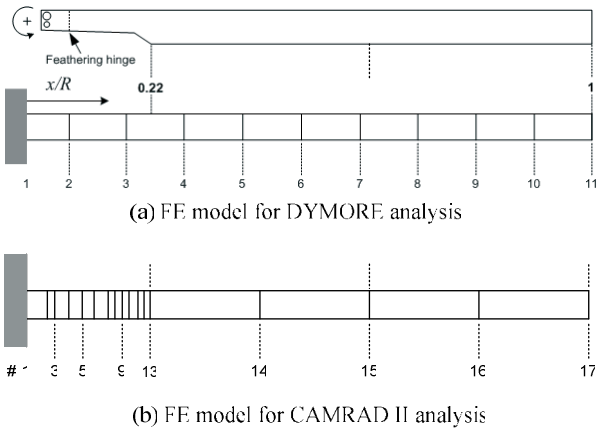

Fig. 1 Finite element model for HART II blades.

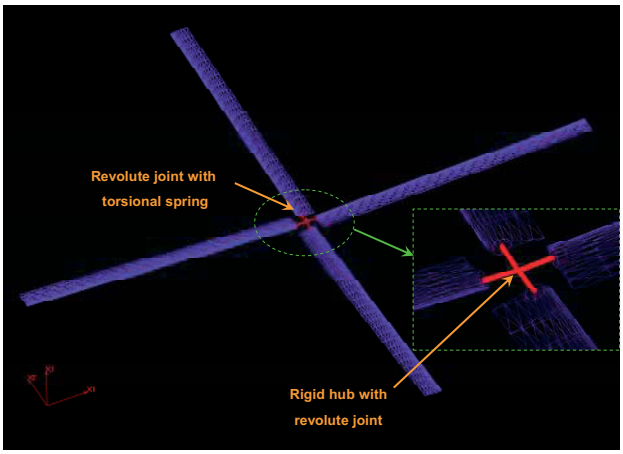

Fig. 2 DYMORE analysis model of HART II rotor.

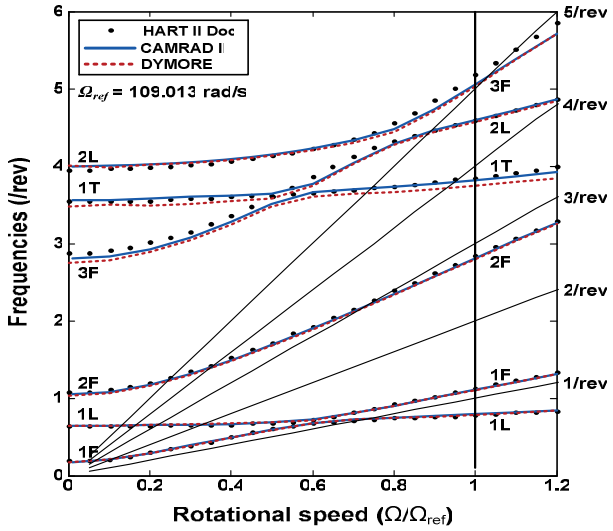

Fig. 3 Comparison of rotating natural frequencies.

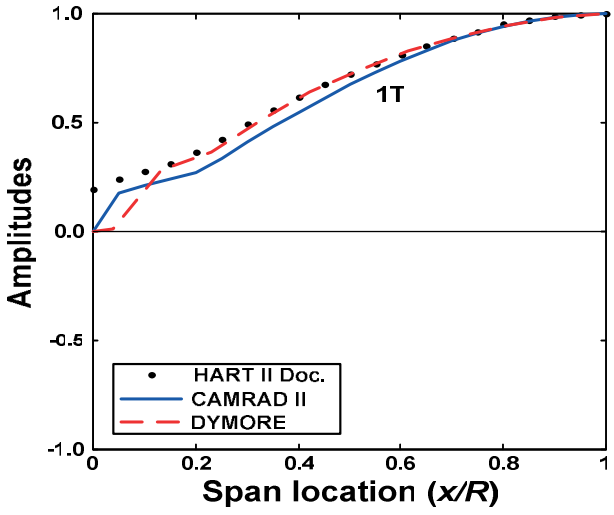

(c) Torsion mode

Fig. 4 Comparison of mode shapes of HART II blades.

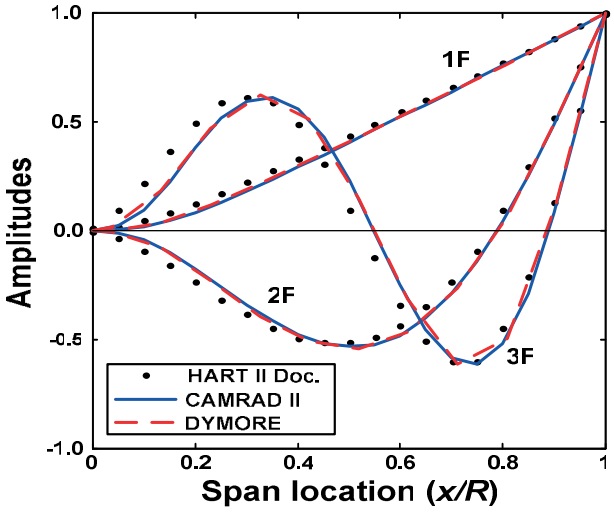

(a) Flap modes

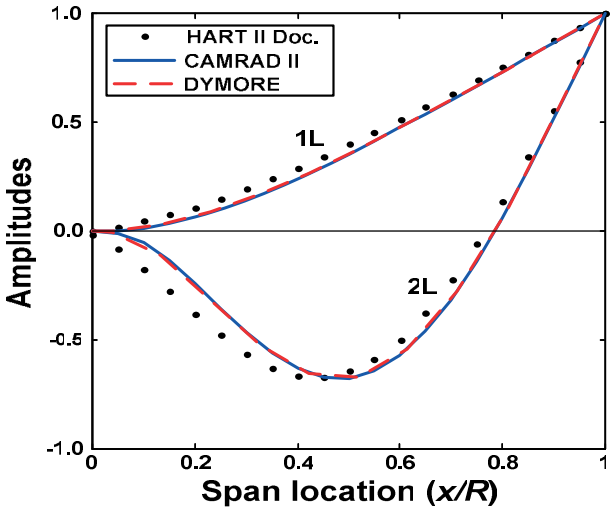

(b) Lead-lag modes

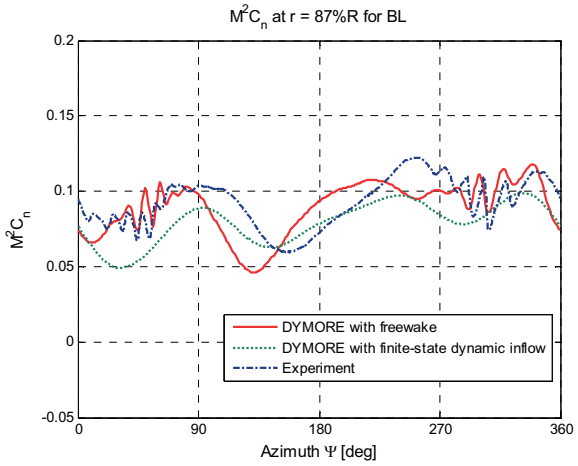

(a) M^2C_n

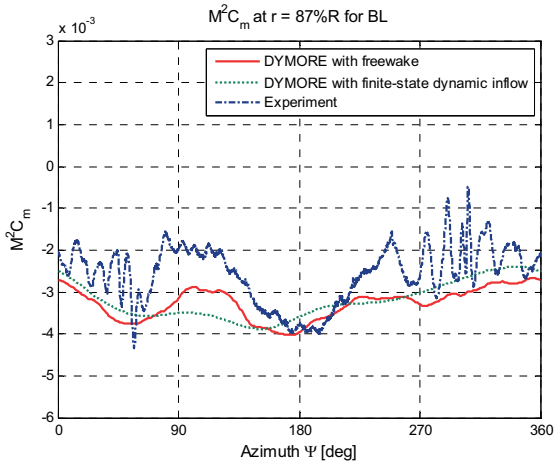

(b) M^2C_m

Fig. 5 Effect of inflow models on section normal forces and pitching moments at 87% station for the BL case.

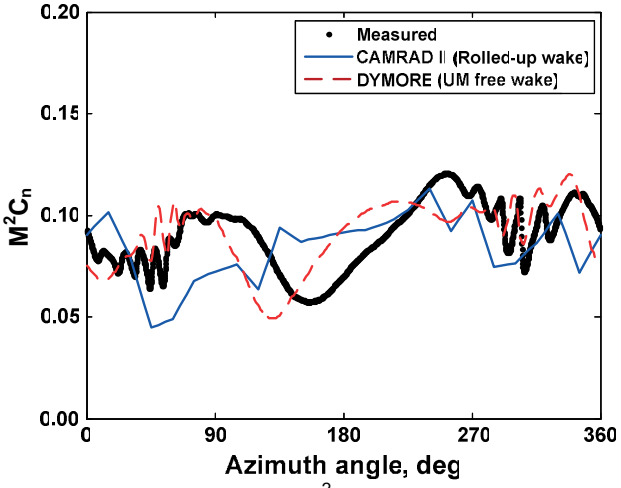

(a) M^2C_n

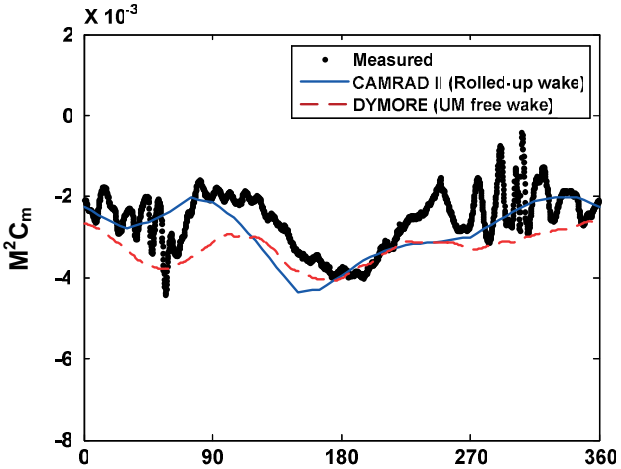

(b) M^2C_m

Fig. 6 Comparison of section normal forces and pitching moments at 87% station for the BL case.

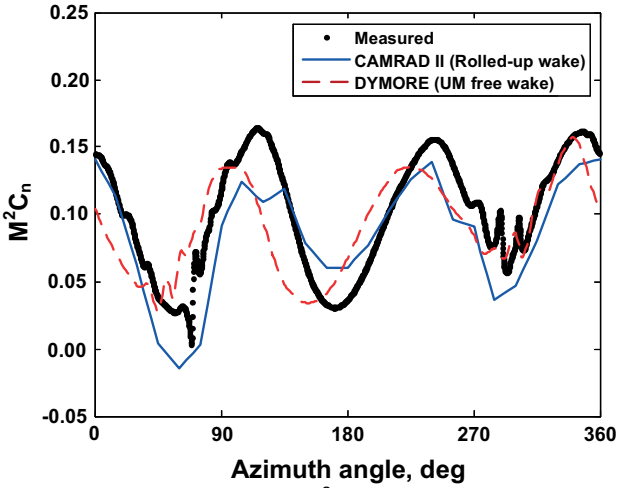

(a) M^2C_n

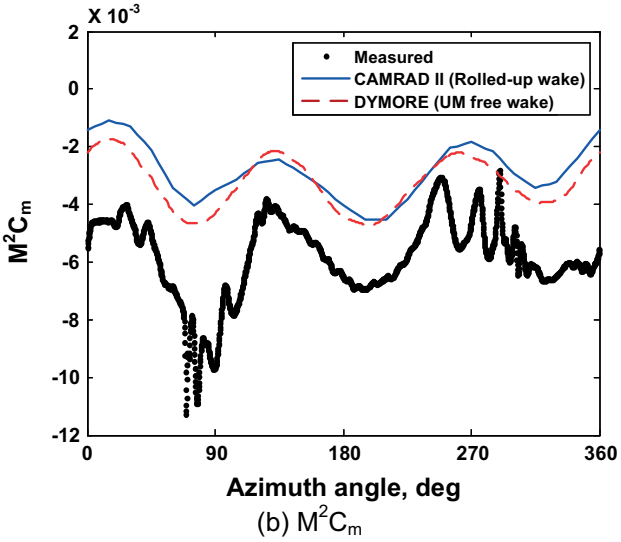

(b) M^2C_m

Fig. 7 Comparison of section normal forces and pitching moments at 87% station for the MN case.

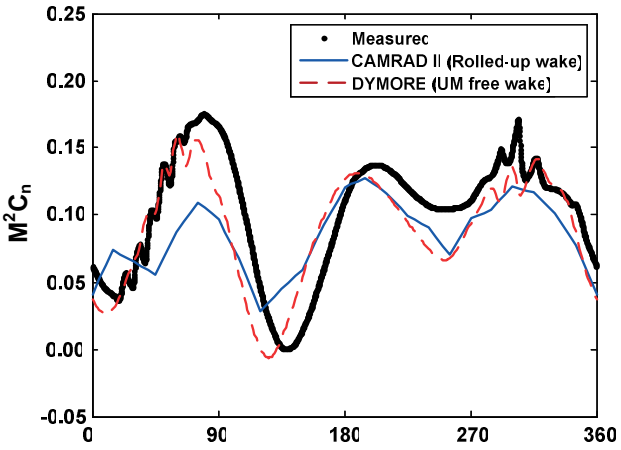

(a) M^2C_n

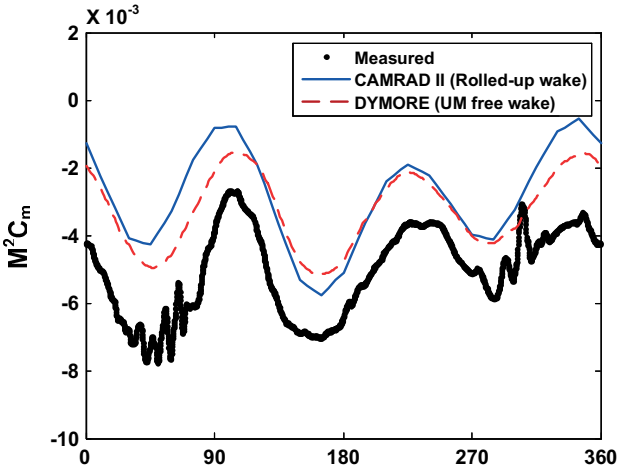

(b) M^2C_m

Fig. 8 Comparison of section normal forces and pitching moments at 87% station for the MV case.

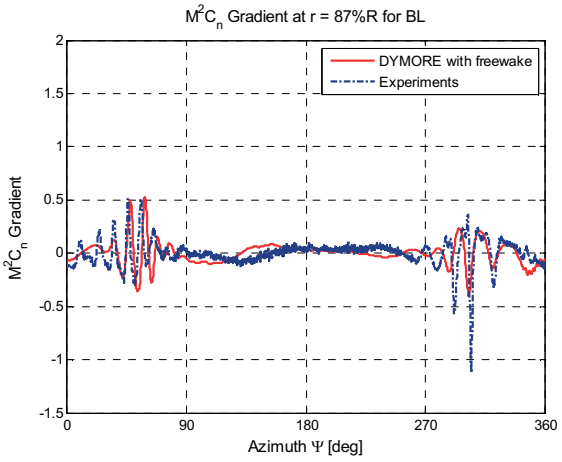

(a) BL case

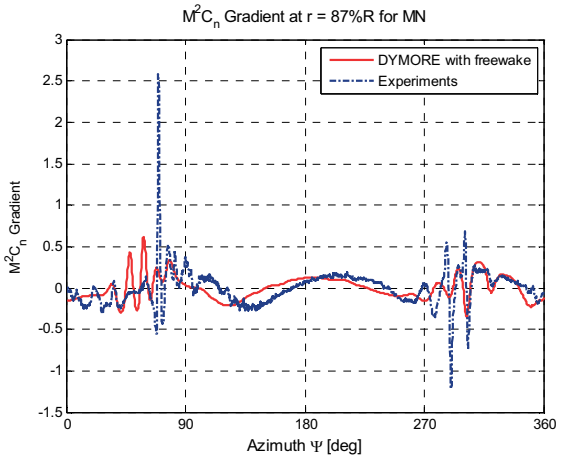

(b) MN case

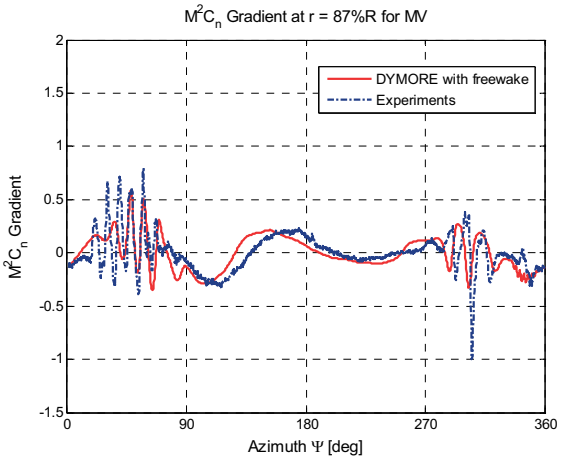

(c) MV case

Fig. 9 Comparison of section lift gradient at 87% radial station for the three cases.

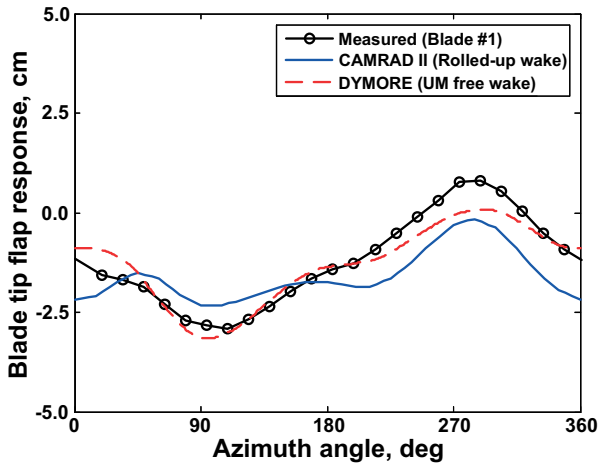

(a) Flap deflection

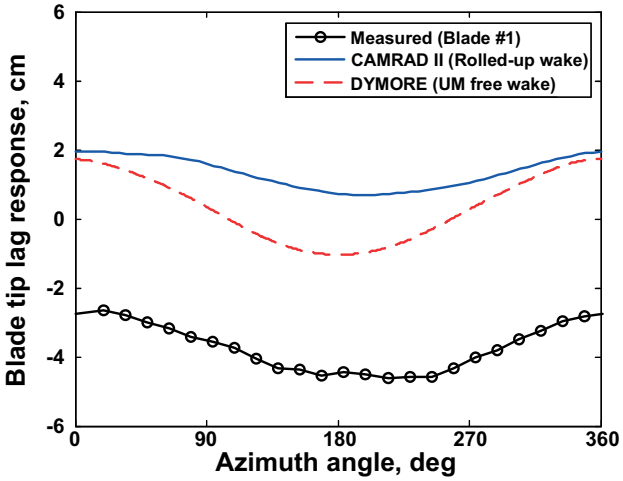

(b) Lead-lag deflection

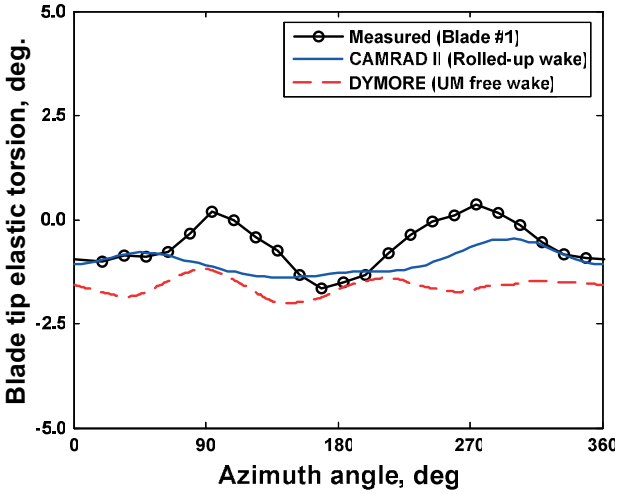

(c) Elastic twist angles

Fig. 10 Comparison of tip displacements for the BL case.

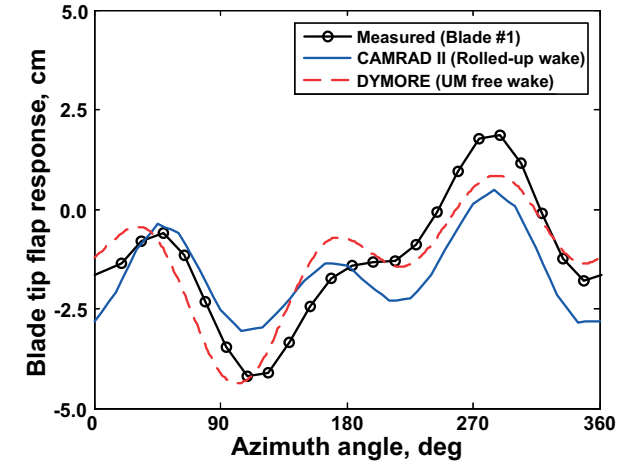

(a) Flap deflection

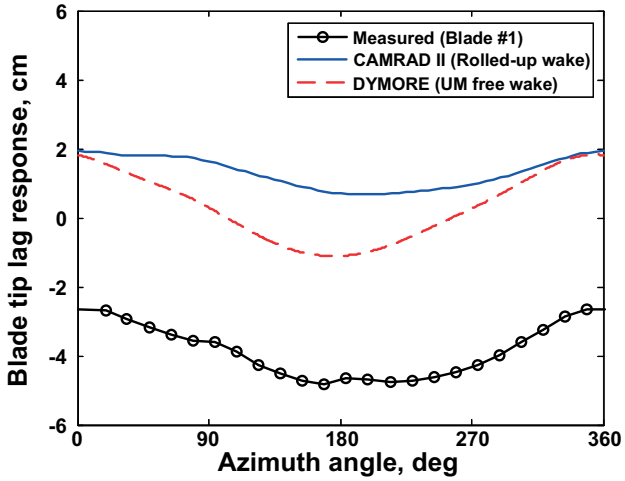

(b) Lead-lag deflection

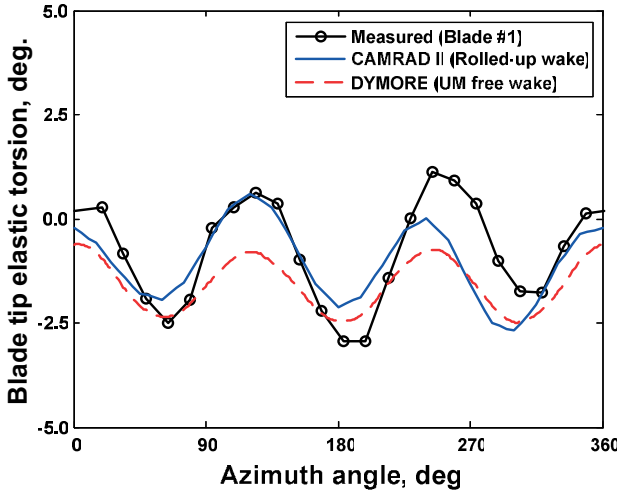

(c) Elastic twist angles

Fig. 11 Comparison of tip displacements for the MN case.

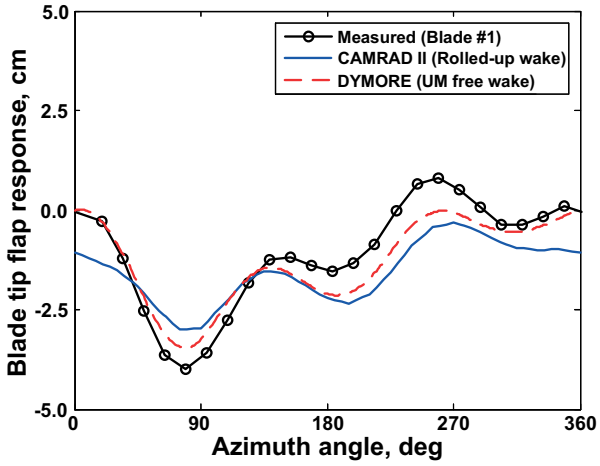

(a) Flap deflection

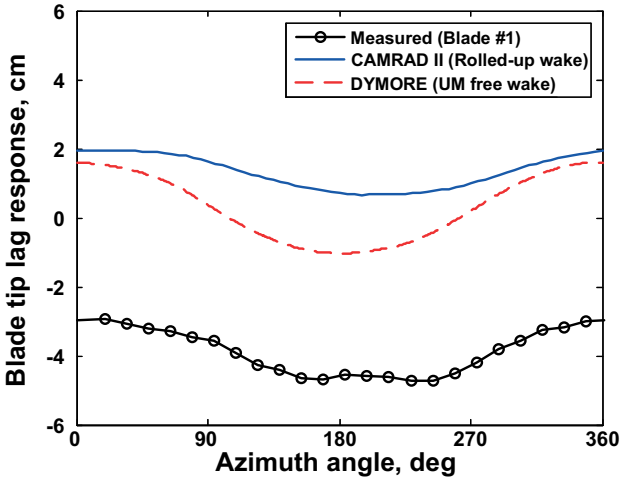

(b) Lead-lag deflection

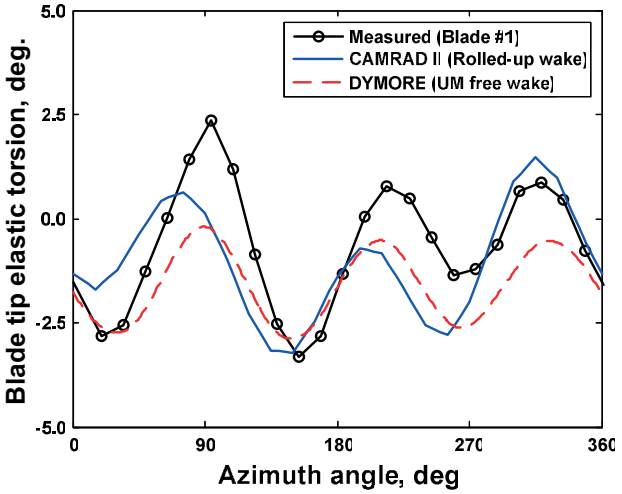

(c) Elastic twist angles

Fig. 12 Comparison of tip displacements for the MV case.

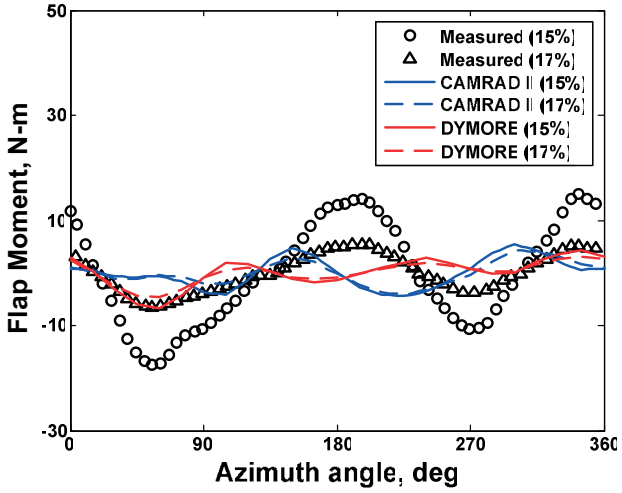

(a) Flap bending

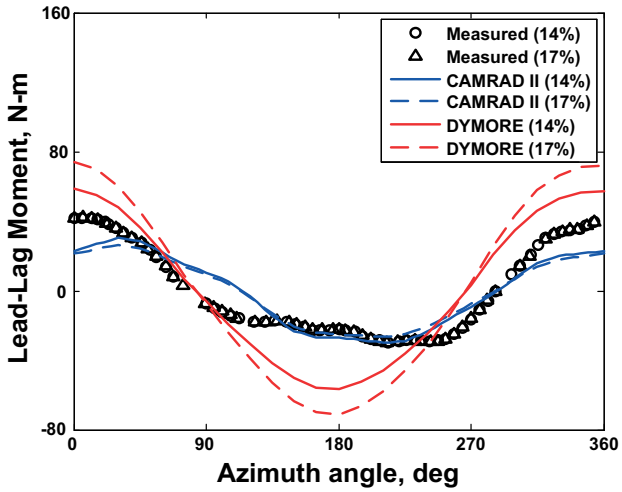

(b) Lead-lag bending

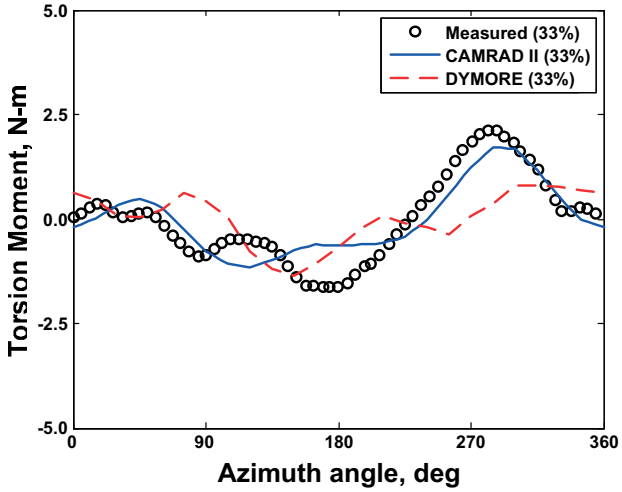

(c) Torsion moment

Fig. 13 Comparison of structural moments for the BL case.

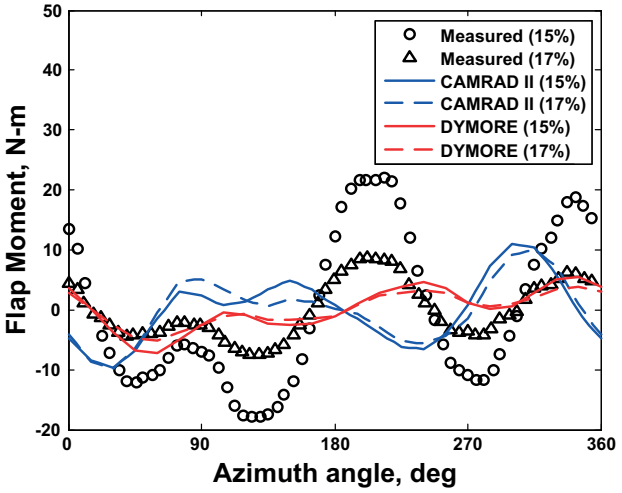

(a) Flap bending

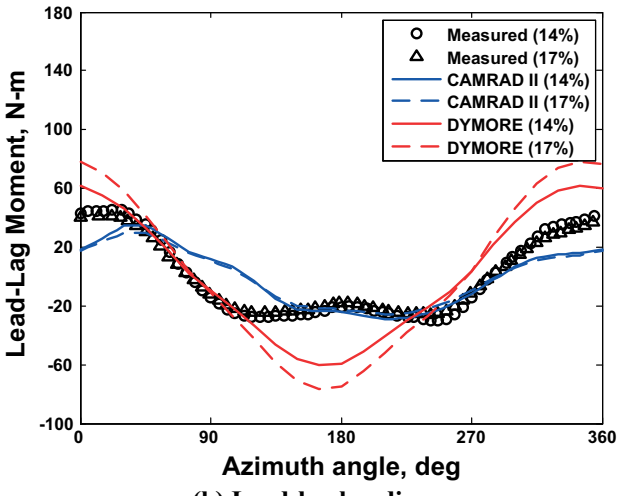

(b) Lead-lag bending

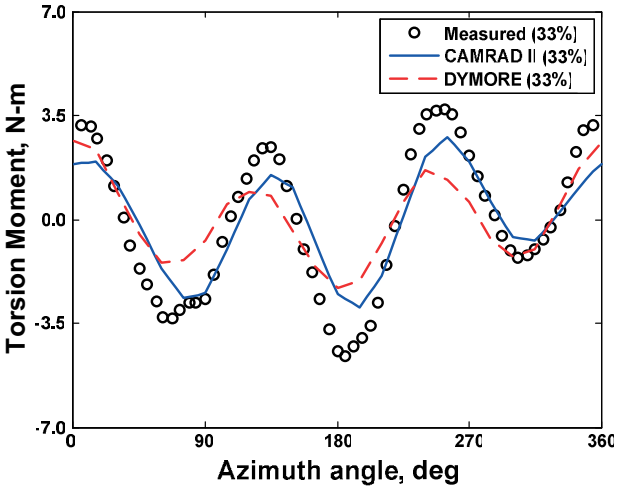

(c) Torsion moment

Fig. 14 Comparison of structural moments for the MN case.

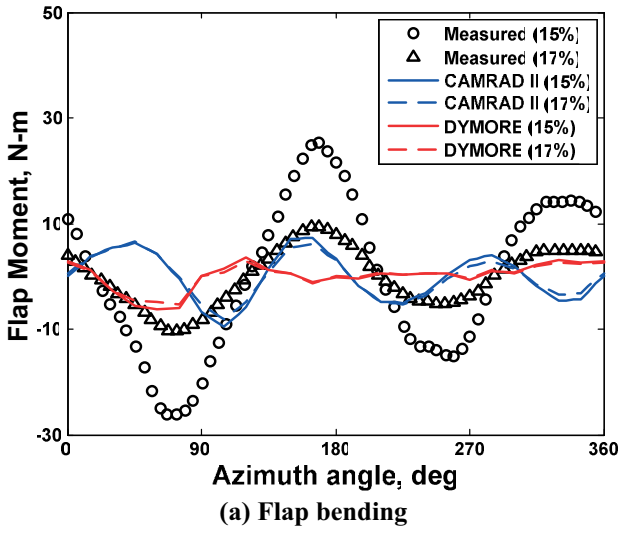

(a) Flap bending

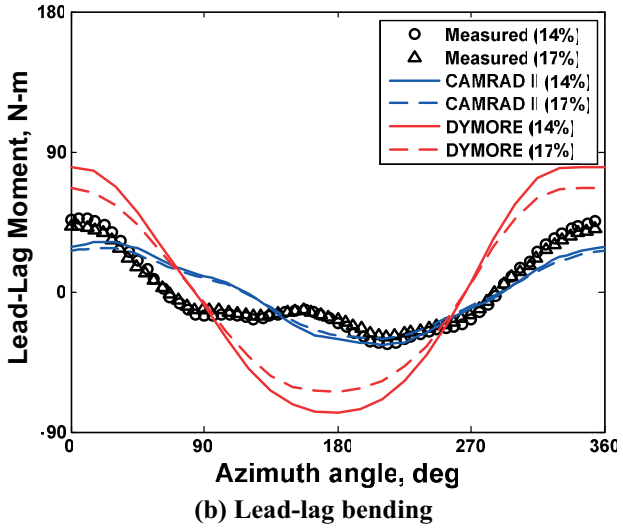

(b) Lead-lag bending

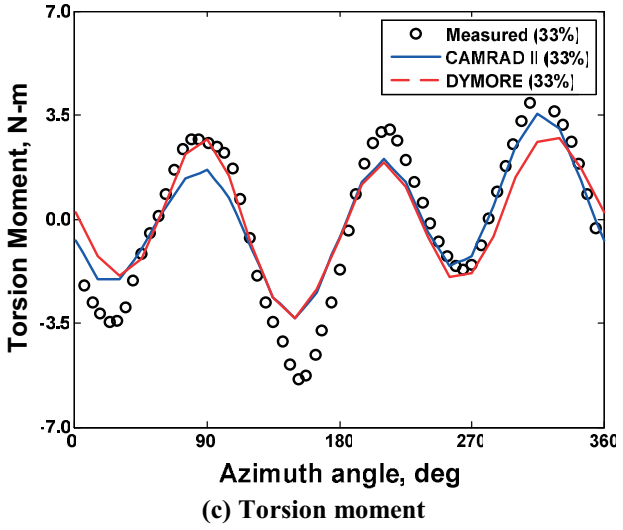

(c) Torsion moment

Fig. 15 Comparison of structural moments for the MV case.